| | |
|---|---|
| Title | Yolk-shell Fe2O3 C composites anchored on MWNTs with enhanced lithium and sodium storage |
| Author(s) | Zhao, Yi; Feng, Zhenxing; Xu, Zhichuan Jason |
| Citation | Zhao, Y., Feng, Z., & Xu, Z. J. (2015). Yolk-shell Fe2O3 C composites anchored on MWNTs with enhanced lithium and sodium storage. Nanoscale, 7(21), 9520-9525. |
| Date | 2015 |
| URL | http://hdl.handle.net/10220/25864 |
| Rights | © 2015 The Royal Society of Chemistry. This is the author created version of a work that has been peer reviewed and accepted for publication by Nanoscale, The Royal Society of Chemistry. It incorporates referee's comments but changes resulting from the publishing process, such as copyediting, structural formatting, may not be reflected in this document. The published version is available at: [http://dx.doi.org/10.1039/C5NR01281C]. |

Journal Name

Dynamic Article Links ►

Cite this: DOI: 10.1039/c0xx00000x

www.rsc.org/xxxxxx

ARTICLE TYPE

# Yolk-shell $Fe_2O_3$⊙C composites anchored on MWNTs with enhanced lithium and sodium storage

**Yi Zhao,[a] Zhenxing Feng,[c] Zhichuan J. Xu[*a, b]**

***Received (in XXX, XXX) Xth XXXXXXXXX 20XX, Accepted Xth XXXXXXXXX 20XX***

**DOI: 10.1039/b000000x**

**A unique architecture with yolk-shell $Fe_2O_3$⊙C composites attached on the surface of MWNTs was designed. Benefiting from the good electrical conductivity of MWNTs and carbon layer, as well as the large void space to accommodate the volume expansion/extraction of $Fe_2O_3$ during battery cycling, the obtained MWNTs@$Fe_2O_3$ ⊙ C exhibited outstanding lithium and sodium storage performance.**

Lithium-ion batteries (LIBs) have attracted increasing attention as dominant power sources for transportation systems and stationary storage of intermittent renewable energies. Thus, there is great demand to design novel LIBs with low cost, good safety, high energy density, and long cycling life.[1-3] Recently, Na-ion batteries (NIBs) have been considered as a new electrochemical system for large-scale energy storage applications due to the low cost and abundant sodium resources.[4, 5] However, the commercial graphite anode are problematic, either leading to a low theoretical capacity of only 372 mAh $g^{-1}$ for LIBs or resulting in the poor intercalation for the large ionic radium of $Na^+$ (0.102 nm). To develop high performance anode materials for next generation batteries, transition metal oxides with high theoretical capacity have been widely studied for LIBs and NIBs.[6-8] Among them, $Fe_2O_3$ has been considered as a promising candidate because of its abundance, low cost, environmental benign, as well as a high theoretical capacity (1007 mAh $g^{-1}$). However, the electrical conductivity of $Fe_2O_3$ is poor (~$7\times10^{-3}$ S $cm^{-1}$). In addition, the large volume changes of $Fe_2O_3$ during Li or Na insertion/extraction processes result in the agglomeration and pulverization problems of active material with fast capacity fading. To mitigate these problems, nanostructured $Fe_2O_3$ with various morphologies has been synthesized. Such nanostructure anodes could provide abundant active site, large surface-to-volume ratio, and short diffusion path for electron and ions to enhance the electrochemical performance.[9-17] For example, Cho et. al reported a mesoporous $Fe_2O_3$ spindle with a high lithium storage of 911 mAh $g^{-1}$ remained after 50 cycles at 0.2 C.[18] A nanosized $Fe_2O_3$ could exhibit sodium storage of 350 mAh $g^{-1}$ at 40 mA $g^{-1}$ after 30 cycles.[19]

Another effective method is to hybrid $Fe_2O_3$ with carbonaceous materials. Carbon materials not only improve the electrical conductivity, but also act as buffering matrix to cushion the mechanical stress caused by the volume expansion/shrinkage of $Fe_2O_3$.[20, 21] The popular carbon materials are carbon coating, porous carbons, carbon nanotubes, graphene, etc.[22-31] For instance, Zhang's group dispersed $Fe_2O_3$ on 3D graphene networks, resulting in a high capacity of 864 mAh $g^{-1}$ after 50 cycles at 200 mA $g^{-1}$ for LIBs.[32] Recently, a porous γ-$Fe_2O_3$@C nanocomposite synthesized by Chen's group exhibited excellent sodium storage performance.[33] Although the composites of $Fe_2O_3$ and carbon showed improved electrochemical behavior, there are still some drawbacks. For example, the amorphous carbon coating gives poor electrical conductivity. Furthermore, due to the large volume changes, the agglomeration and pulverization problems on graphene and carbon nanotubes were inevitable. Therefore, a solution is to combine $Fe_2O_3$ with hybrid carbon nanomaterials to design superior anode materials.[34-39] Recently, $Fe_2O_3$@C composite distributed on graphene exhibited good cycling performance with a high capacity of 864 mAh $g^{-1}$ after 100 cycles.[40] It is also noted that γ-$Fe_2O_3$ as an example, the volume changes for lithium and sodium storage were 80 % and 190 %, respectively. Thus, the void space should be reserved in the composites of $Fe_2O_3$ and hybrid carbons, to accommodate the volume changes for long-term cycling life.

Here, we designed a novel architecture with yolk-shell $Fe_2O_3$⊙C composites anchored on the surface of multi-walled carbon nanotubes (MWNTs), denoted as MWNTs@ $Fe_2O_3$⊙C, with multi-purposes to improve the electrical conductivity, prevent the aggregation of active material, and provide large interior void space for accommodating the volume changes of $Fe_2O_3$ during cycles. As anode materials for LIBs and NIBs, the MWNTs@ $Fe_2O_3$⊙C electrode exhibited outstanding electrochemical performance. For lithium storage, this electrode was able to remain high specific capacities of 1024 and 502 mAh $g^{-1}$ after 360 cycles, when cycled at 200 and 2000 mA $g^{-1}$, respectively. For sodium storage, this composite also delivered excellent rate capabilities and good cycling stability.

Fig. 1a illustrated the scheme for the fabrication of MWNTs@$Fe_2O_3$⊙C composite. First, FeOOH nanorods were assembled on the surface of acid-MWNTs with high loading ratio by a simple hydrolysis of $FeCl_3$.[34] In the second step, the MWNTs@FeOOH composite was coated with a $SiO_2$ layer via a modified StÖber method, to control the void space in the final composite. Third, a carbon layer was achieved by the coating of a resorcinol–formaldehyde (RF) resin layer and then carbonized at 700 ℃ for 2h under Ar.[41] In the last step, by etching the $SiO_2$ layer with NaOH solution, the final product with yolk-shell $Fe_2O_3$⊙C composites anchored on MWNTs can be obtained. Fig.

Cite this: DOI: 10.1039/c0xx00000x

www.rsc.org/xxxxxx

ARTICLE TYPE

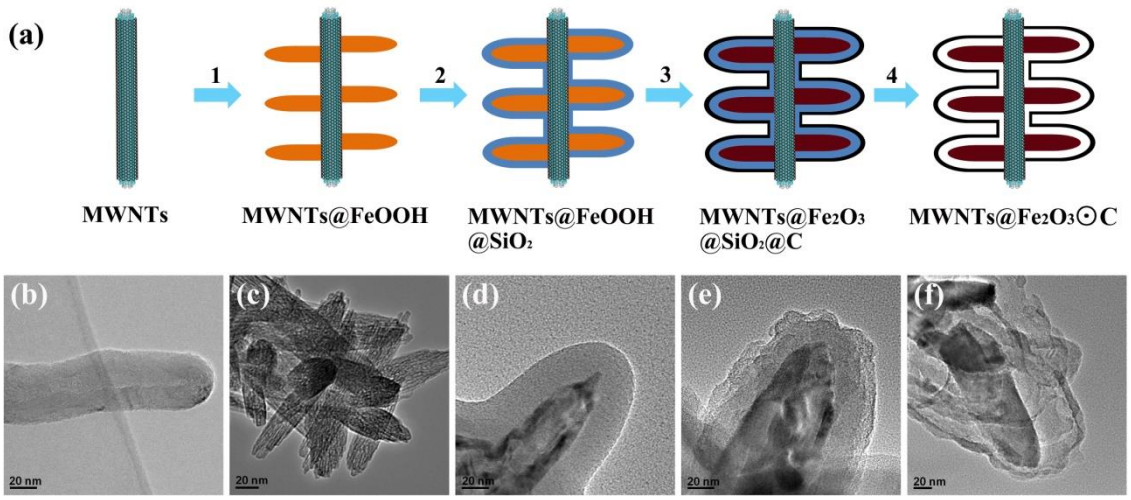


**Fig. 1** (a) Schematic illustration for the fabrication of MWNTs@$Fe_2O_3$⊙C composite. (b-f) are the corresponding TEM images for each product.

1 b-f shows the corresponding high magnification TEM images for each product, which matches well with the design in the scheme.

The structure and morphology of the obtained composites were investigated by SEM and TEM in details. Fig. 2a and b are the SEM and TEM images of the MWNTs@FeOOH composite, revealing the one-dimensional morphology of this composite with high density FeOOH nanorods (width of 20-40 nm and length of

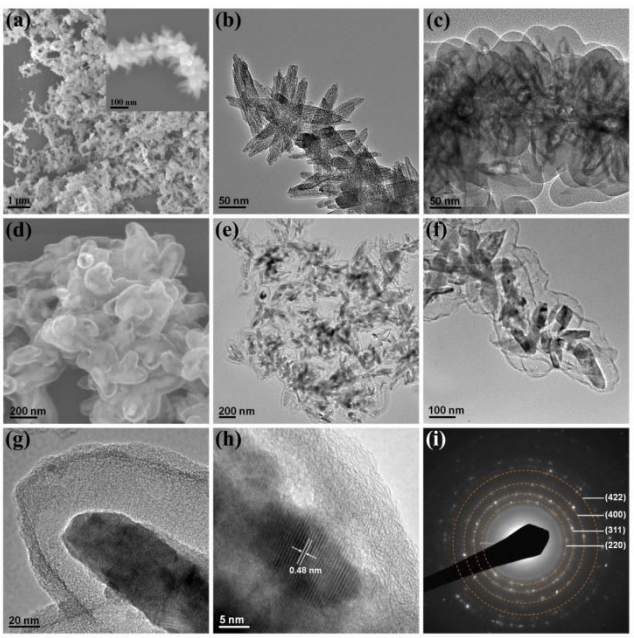


**Fig. 2** (a) SEM and (b) TEM images of MWNTs@FeOOH composite. (c) TEM image of MWNTs@FeOOH@$SiO_2$ composite. (d) SEM and (e-g) TEM images of MWNTs@$Fe_2O_3$⊙C, revealing the formation of yolk-shell $Fe_2O_3$⊙C composite on MWNTs. (h) HRTEM image and (i) corresponding SAED pattern for the well crystallized γ-$Fe_2O_3$ particle.

60-100 nm) anchored on the surface of MWNTs. The high magnification TEM image (Fig. 1c) and the XRD pattern (Fig. S1) further confirmed the tetragonal β-FeOOH with porous structure. The TEM (Fig. 1d and 2c) and SEM (Fig. S2) images of the MWNTs@FeOOH@$SiO_2$ composite disclosed the uniform $SiO_2$ coating on MWNTs@FeOOH composite with a thickness around 15-25 nm. Then, this composite was coated with a carbon layer (Fig. 1e), followed with the removal of $SiO_2$ layer to obtain the final MWNTs@$Fe_2O_3$⊙C composite. Fig. 2d-g and 1f display the SEM and TEM images of this composite, from which the $Fe_2O_3$⊙C composites with void space attached on MWNTs can be clearly observed. The element mappings in Fig. S3 further illustrated the unique architecture of this composite. The thickness of carbon layer was ~10 nm. The high resolution TEM image in Fig. 2h clearly presented the lattice fringes with an interlayer spacing of 0.48 nm, ascribed to the (111) planes of cubic γ-$Fe_2O_3$. The selected area electron diffraction (SAED) pattern in Fig. 2i also confirmed the crystalline characteristics of maghemite nanoparticles, from which the diffraction rings were attributed to the (220), (311), (400), and (422) planes of γ-$Fe_2O_3$.

Fig. 3a exhibits the X-ray diffraction (XRD) pattern of the MWNTs@$Fe_2O_3$⊙C composite. All diffraction peaks in the XRD profile can be well indexed to γ-$Fe_2O_3$ (JCPDS No. 39-1346), in consistence with the TEM observation. The diffraction of MWNTs overlapped with the (211) plane from $Fe_2O_3$. Note that the composite by directly annealing of the MWNTs@FeOOH at 700 ℃, instead of the annealing of the material with the protection of $SiO_2$ and carbon layer, leaded to the formation of face-centered-cubic $Fe_3O_4$, as revealed by XRD (Fig. S4). The peaks of MWNTs@$Fe_3O_4$ were sharper than those of the MWNTs@$Fe_2O_3$⊙C composite, indicating the aggregation of $Fe_3O_4$ particles during calcination process, which was further revealed by the SEM images in Fig. S5. The TGA was carried out to identify the loading ratio of $Fe_2O_3$ in this composite. As shown

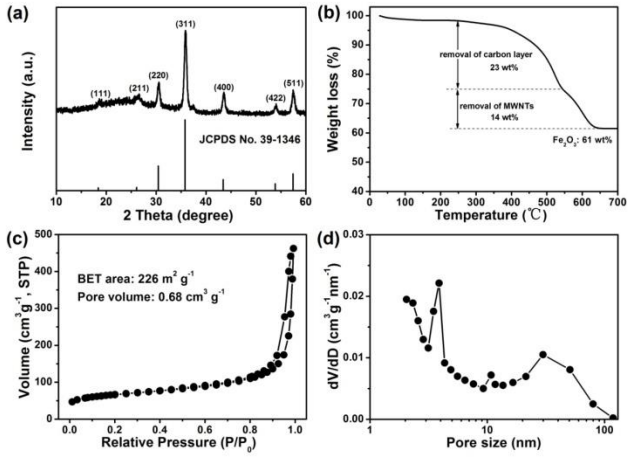


**Fig. 3** (a) XRD pattern, (b) TGA curve, (c) nitrogen adsorption—desorption isotherms, and (d) pore size distribution of the MWNTs@$Fe_2O_3$⊙C composite.

in Fig. 3b, two distinct regions of weight loss can be identified at 250-540 and 540-650 ℃, corresponding to the removal of carbon layer (23 wt%) and MWNTs (14 wt%), respectively.[42] The final content of $Fe_2O_3$ in this composite was about 61 wt%.

The nitrogen adsorption-desorption isotherms experiments of MWNTs@$Fe_2O_3$⊙C composite as shown in Fig. 3c, giving a high BET surface area of 226 $m^2$ $g^{-1}$ and a large pore volume of 0.68 $cm^3$ $g^{-1}$. These are advantageous to provide large electrolyte/electrode contact area and enough void space to tolerate the volume changes of $Fe_2O_3$, thus benefiting for the superior lithium and sodium storage performance. The pore size distribution curve in Fig. 3d exhibited small mesoporous peaks at 2.0 and 3.9 nm as well as a large mesoporous peak around 30 nm, which could be resulted from the mesoporous structure of $Fe_2O_3$ and the void space generated by the removal of $SiO_2$ layer. However, the MWNTs@$Fe_3O_4$ composite that was obtained without the protection of $SiO_2$ and carbon layer only exhibited a BET surface area of 26 $m^2$ $g^{-1}$ and a small pore volume of 0.08 $cm^3$ $g^{-1}$ (Fig. S6).

Fig. 4 illustrates the excellent electrochemical performance of MWNTs@$Fe_2O_3$⊙C composite as an anode material for LIBs. The electrochemical behavior of this composite was firstly studied via cyclic voltammograms (CVs) at 0.5 mV $s^{-1}$ under a voltage range of 0.05-3.00 V in Fig. 4a. In the first cathodic curve, three reduction peaks located around 1.5 V, 1.0 V, and 0.55 V were observed, corresponding to the lithium insertion into $Fe_2O_3$ structure, reduction of $Fe^{3+}$ to $Fe^{2+}$, and further conversion of $Fe^{2+}$ to Fe as well as the formation of solid electrolyte interface (SEI) layer, respectively.[43-47] The intensities of cathodic peaks in the second cycle dropped significantly, indicating the irreversible formation of an SEI film. The voltage region from 1.2 to 2.5 V in the anodic curves was corresponded to the reversible oxidation of Fe to $Fe^{3+}$. After the first cycle, the reduction peaks for $Fe^{3+}$ to $Fe^{2+}$ and $Fe^{2+}$ to $Fe^0$ shifted to higher voltages at 0.75 V and 1.3 V, which can be attributed to the improved kinetics of $Fe_2O_3$ electrode after the structure rearrangement and electrochemical activation. Moreover, the overlapping of the CV curves in the following cycles indicated the highly reversibility of reaction (1).

$$Fe_2O_3 + 6Li^+ + 6e^- \leftrightarrow 2Fe + 3Li_2O \quad (1)$$

Fig. 4b displays the initial three discharge/charge profiles of MWNTs@$Fe_2O_3$⊙C at 200 mA $g^{-1}$. The voltage plateaus as clearly observed in these profiles corresponded to the reversible conversion between $Fe_2O_3$ and Fe, in consistence with results from the CVs measurements. The initial discharge and charge curves delivered capacities of 1389 and 896 mAh $g^{-1}$ with a columbic efficiency of 64.5%. The capacity loss in the first cycles was mainly ascribed to irreversible decomposition of electrolyte to form SEI layer (the slopped voltage region below 0.8 V). Fig. 4c discloses the excellent cycling performance of the MWNTs@$Fe_2O_3$⊙C electrode. After 360 successive cycles, this electrode still delivered a high charge capacity of 1024 mAh $g^{-1}$ at a current density of 200 mA $g^{-1}$. Considering the theoretical capacity of $Fe_2O_3$ (1007 mAh $g^{-1}$) and the loading ratio of $Fe_2O_3$ in this composite (61 wt%), the obtained capacity is much higher than the theoretical value for MWNTs@$Fe_2O_3$⊙C composite. The possible reason from this extra capacity could be due to the reversible formation of polymeric gel-like film as well as the interfacial storage of excess lithium ions between primary nanoparticles, which have been often observed in other iron oxide composites.[14, 24, 48] Moreover, this electrode also presented good cycling retention at a high rate of 2000 mA $g^{-1}$ after being activated at 200 mA $g^{-1}$ in the first two cycles, which remained a high capacity of 502 mAh $g^{-1}$ after 360 cycles. Meanwhile, the columbic efficiency kept around 99% during cycles.

Fig. 4d reveals the outstanding rate capabilities of this electrode. The typical discharge/charge curves under various rates were showed in Fig. S7, which remained the electrochemical reaction plateaus and delivered high capacities even at high rates.

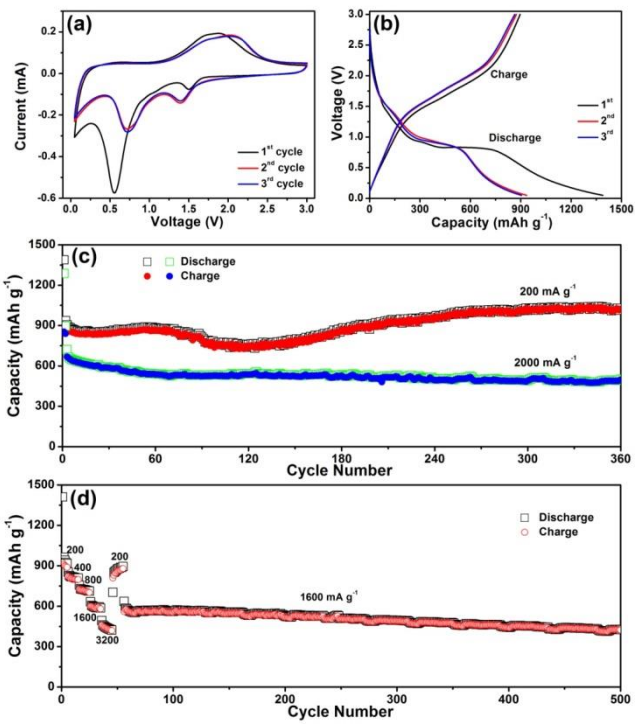


**Fig. 4** Electrochemical performance of MWNTs@$Fe_2O_3$⊙C anode for LIBs. (a) CV curves at a scan rate of 0.5 mV $s^{-1}$ from 0.05 V to 3.00 V, (b) discharge/charge curves of initial three cycles at 200 mA $g^{-1}$, (c) cycling performance at 200 and 2000 mA $g^{-1}$, (d) rate capabilities at various current densities from 200 to 3200 mA $g^{-1}$.

The MWNTs@$Fe_2O_3$⊙C electrode was able to deliver high specific capacities of 828, 756, 633, and 493 mAh $g^{-1}$ when cycled at 400, 800, 1600, and 3200 mA $g^{-1}$, respectively. When the current density reduced back to 200 mA $g^{-1}$, a high capacity of 890 mAh $g^{-1}$ was recovered, indicating the good structure stability of MWNTs@$Fe_2O_3$⊙C electrode. In addition, even after various discharge/charge rates test, this electrode still presented excellent cycling retention at a high rate of 1.6 A $g^{-1}$, with a charge capacity of 423 mAh $g^{-1}$ after 500 cycles and a low capacity loss of 0.05% per cycle. Compared with the previous reported composites with $Fe_2O_3$/$Fe_3O_4$@C anchored on MWNTs or graphene,[34, 36, 40, 49] our obtained MWNTs@$Fe_2O_3$⊙C showed improved cycling performance. This could be attributed to the large void space in this composite to accommodate the volume expansion of $Fe_2O_3$ during cycles with good structure stability.[50-53]

The lithium storage performance test of the MWNTs@$Fe_3O_4$ composite was also performed (Fig. S8). Due to the large particle size of $Fe_3O_4$, this composite only exhibited low initial discharge and charge capacities of 1047 and 690 mAh $g^{-1}$ at 200 mA $g^{-1}$. Without the protection of void space and carbon layer, the MWNTs@$Fe_3O_4$ anode suffered from the gradual capacity fading with a low capacity of 180 mAh $g^{-1}$ after 400 cycles at 2000 mA $g^{-1}$. The comparison studies on MWNTs@$Fe_3O_4$ and MWNTs@$Fe_2O_3$⊙C showed that the outstanding lithium storage performance of latter material could be ascribed to the following reasons. First, the MWNTs and carbon layer resulted in the high electrical conductivity in this composite (Fig. S9). Furthermore, the high surface area of this composite and the nanosized $Fe_2O_3$ provided large electrode/electrolyte contact area and short path length for $Li^+$ transport, thus benefiting for the high specific capacity and good rate performance of this composite. Second, the carbon coating effectively prevented the aggregation and pulverization of $Fe_2O_3$ during cycling. Third, the large pore volume of the MWNTs@$Fe_2O_3$ ⊙ C composite can provide enough void space to accommodate the volume expansion of $Fe_2O_3$ during lithium insertion/extraction processes, resulting in good structure stability with outstanding cycling performance (Fig. S10).

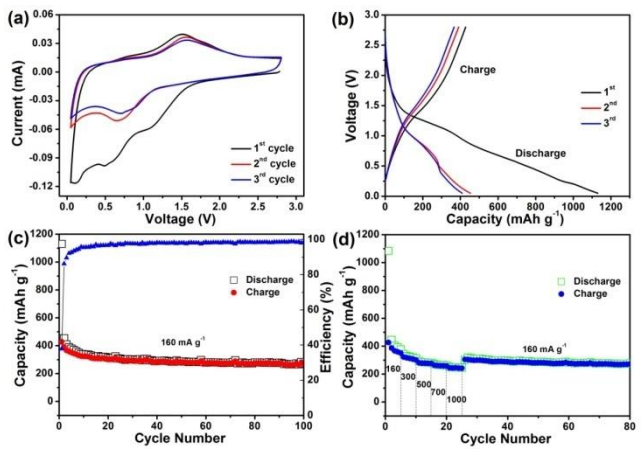


**Fig. 5** Electrochemical characterization of MWNTs@$Fe_2O_3$⊙C anode for NIBs. (a) CVs curves at 0.5 mV $s^{-1}$ between 0.05 and 2.8 V, (b) discharge/charge profiles for the initial three cycles at 160 mA $g^{-1}$, (c) cycling stability at 160 mA $g^{-1}$, and (d) rate performance at various rates from 160 to 1000 mA $g^{-1}$.

The unique architecture of MWNTs@$Fe_2O_3$⊙C composite also benefits the superior sodium storage performance. Fig. 5a shows the CVs curves of this electrode at 0.5 mV $s^{-1}$. In the initial cathodic process, a reduction peak around 1.1 V was detected, which may be due to the Na insertion into $Fe_2O_3$ structure and the formation of $Na_xFe_2O_3$. Another broad cathodic peaks at 0.5 V was ascribed to the reduction of $Fe_2O_3$ into Fe, accompanied with the formation of SEI layer. The large difference between the first cycle and the following cycles was due to the irreversible formation of SEI layer. In the following cycles, a characteristic redox pair located at around (cathodic/anodic) 0.7/1.5 V was attributed to the reversible conversion between $Fe_2O_3$ and Fe in reaction (2).[33, 54]

$$Fe_2O_3 + 6Na^+ + 6e^- \leftrightarrow 2Fe + 3Na_2O \quad (2)$$

Fig. 5b presents the discharge/charge profiles of the MWNTs@$Fe_2O_3$⊙C electrode at 160 mA $g^{-1}$. Compared with the discharge/charge profiles for LIBs in Fig. 4b, the plateaus for NIBs in these profiles were not obvious. This could be due to the large $Na^+$ ionic size that resulted in the sluggish kinetic of sodium insertion/extraction process. The initial discharge/charge capacities of this electrode were 1130 and 427 mAh $g^{-1}$, respectively. This large capacity loss was mainly due to the irreversible formation of SEI layer, in consistence with the CVs observation in Fig. 5a. Fig. 5c displays the good cycling performance of MWNTs@$Fe_2O_3$⊙C electrode, which remained a discharge capacity of 272 mAh $g^{-1}$ after 100 cycles with a columbic efficiency around 98 % during cycles. While, the MWNTs@$Fe_3O_4$ electrode only exhibited a low capacity of ~30 mAh $g^{-1}$ at 160 mA $g^{-1}$ after 100 cycles (Fig. S11). The excellent rate capabilities of MWNTs@$Fe_2O_3$⊙C anode are also revealed in Fig. 5d. It delivered a high discharge capacity of 251 mAh $g^{-1}$ even at a large current density of 1000 mA $g^{-1}$, which was higher than the value for graphene@$Fe_2O_3$ composite.[30] When the current density was lowered back to 160 mAh $g^{-1}$, a high capacity of 310 mAh $g^{-1}$ can be recovered and remained high capacity retention of 90% up to 80 cycles. Compared with the previous reported iron oxides for NIBs (Table. S1), our composite also delivered superior cycling performance with cycling number up to 600 cycles (Fig. S12).

In summary, a novel architecture with yolk-shell $Fe_2O_3$⊙C composites anchored on MWNTs has been designed and fabricated for high performance LIBs and NIBs. Due to the good electrical conductivity of MWNTs and carbon layer, as well as the void space to tolerate the volume changes of $Fe_2O_3$ during cycles, the obtained MWNTs@$Fe_2O_3$⊙C composite delivered high specific capacity, good rate performance, and excellent cycling stability for both lithium and sodium storage. This strategy by dispersing electrode materials within hybrid carbons with interior void space can also be applied to other energy storage systems such as Mg-ion batteries for the improved performance.

This work was supported by the Start-Up Grant of Nanyang Technological University, and the Singapore MOE Tier 1 Grants (RGT8/13 and RG13/13) and the Singapore National Research Foundation under its Campus for Research Excellence And Technological Enterprise (CREATE) programme.

## Notes and references

[a]School of Materials Science and Engineering, Nanyang Technological University, Singapore 639798, Singapore
E-mail: xuzc@ntu.edu.sg
[b]Energy Research Institute @ NTU, Nanyang Technological University, 50 Nanyang Drive, Singapore, Singapore 639798, Singapore
[c]Chemical Science and Engineering Division, Argonne National Laboratory, Argonne, IL, 60439, United States

† Electronic Supplementary Information (ESI) available: [details of any supplementary information available should be included here]. See DOI: 10.1039/b000000x/

1. M. Armand and J. M. Tarascon, *Nature*, 2008, **451**, 652.
2. F. Y. Cheng, J. Liang, Z. L. Tao and J. Chen, *Adv. Mater.*, 2011, **23**, 1695.
3. N. S. Choi, Z. H. Chen, S. A. Freunberger, X. L. Ji, Y. K. Sun, K. Amine, G. Yushin, L. F. Nazar, J. Cho and P. G. Bruce, *Angew. Chem. Int. Ed.*, 2012, **51**, 9994.
4. M. D. Slater, D. Kim, E. Lee and C. S. Johnson, *Adv. Funct. Mater.*, 2013, **23**, 947.
5. N. Yabuuchi, K. Kubota, M. Dahbi and S. Komaba, *Chem. Rev.*, 2014, **114**, 11636.
6. P. Poizot, S. Laruelle, S. Grugeon, L. Dupont and J. M. Tarascon, *Nature*, 2000, **407**, 496.
7. M. V. Reddy, G. V. S. Rao and B. V. R. Chowdari, *Chem. Rev.*, 2013, **113**, 5364.
8. Y. Kim, K. H. Ha, S. M. Oh and K. T. Lee, *Chem. Eur. J.*, 2014, **20**, 11980.
9. P. G. Bruce, B. Scrosati and J. M. Tarascon, *Angew. Chem. Int. Ed.*, 2008, **47**, 2930.
10. J. Chen, L. N. Xu, W. Y. Li and X. L. Gou, *Adv. Mater.*, 2005, **17**, 582.
11. M. V. Reddy, T. Yu, C. H. Sow, Z. X. Shen, C. T. Lim, G. V. S. Rao and B. V. R. Chowdari, *Adv. Funct. Mater.*, 2007, **17**, 2792.
12. J. S. Chen, T. Zhu, X. H. Yang, H. G. Yang and X. W. Lou, *J. Am. Chem. Soc.*, 2010, **132**, 13162.
13. J. X. Zhu, Z. Y. Yin, D. Yang, T. Sun, H. Yu, H. E. Hoster, H. H. Hng, H. Zhang and Q. Y. Yan, *Energ. Environ. Sci.*, 2013, **6**, 987.
14. S. M. Xu, C. M. Hessel, H. Ren, R. B. Yu, Q. Jin, M. Yang, H. J. Zhao and D. Wang, *Energ. Environ. Sci.*, 2014, **7**, 632.
15. S. Komaba, T. Mikumo, N. Yabuuchi, A. Ogata, H. Yoshida and Y. Yamada, *J. Electrochem. Soc.*, 2010, **157**, A60.
16. L. Li, H. B. Wu, L. Yu, S. Madhavi and X. W. D. Lou, *Adv. Mater. Interfaces*, 2014, **1**, 1400050.
17. K. Cao, L. Jiao, H. Liu, Y. Liu, Y. Wang, Z. Guo and H. Yuan, *Adv. Energy Mater.*, 2014, **5**, 1401421.
18. X. Xu, R. Cao, S. Jeong and J. Cho, *Nano Lett.*, 2012, **12**, 4988.
19. M. Valvo, F. Lindgren, U. Lafont, F. Bjorefors and K. Edstrom, *J. Power Sources*, 2014, **245**, 967.
20. S. L. Candelaria, Y. Y. Shao, W. Zhou, X. L. Li, J. Xiao, J. G. Zhang, Y. Wang, J. Liu, J. H. Li and G. Z. Cao, *Nano Energy*, 2012, **1**, 195.
21. C. J. Shearer, A. Cherevan and D. Eder, *Adv. Mater.*, 2014, **26**, 2295.
22. Y. Zhao, J. X. Li, C. X. Wu and L. H. Guan, *Nanoscale Res. Lett.*, 2011, **6**, 71.
23. T. Yoon, C. Chae, Y. K. Sun, X. Zhao, H. H. Kung and J. K. Lee, *J. Mater. Chem.*, 2011, **21**, 17325.
24. Y. Zhao, J. X. Li, Y. H. Ding and L. H. Guan, *Chem. Commun.*, 2011, **47**, 7416.
25. J. Lin, A. R. O. Raji, K. W. Nan, Z. W. Peng, Z. Yan, E. L. G. Samuel, D. Natelson and J. M. Tour, *Adv. Funct. Mater.*, 2014, **24**, 2044.
26. N. Yan, X. H. Zhou, Y. Li, F. Wang, H. Zhong, H. Wang and Q. W. Chen, *Sci. Rep.*, 2013, **3**, 3392.
27. H. W. Zhang, L. Zhou, O. Noonan, D. J. Martin, A. K. Whittaker and C. Z. Yu, *Adv. Funct. Mater.*, 2014, **24**, 4337.
28. X. Gu, L. Chen, S. Liu, H. Y. Xu, J. Yang and Y. T. Qian, *J. Mater. Chem. A*, 2014, **2**, 3439.
29. R. H. Wang, C. H. Xu, M. Du, J. Sun, L. Gao, P. Zhang, H. L. Yao and C. C. Lin, *Small*, 2014, **10**, 2260.
30. Z. L. Jian, B. Zhao, P. Liu, F. J. Li, M. B. Zheng, M. W. Chen, Y. Shi and H. S. Zhou, *Chem. Commun.*, 2014, **50**, 1215.
31. Y. Zhao, J. X. Li, Y. H. Ding and L. H. Guan, *J. Mater. Chem.*, 2011, **21**, 19101.
32. X. H. Cao, B. Zheng, X. H. Rui, W. H. Shi, Q. Y. Yan and H. Zhang, *Angew. Chem. Int. Ed.*, 2014, **53**, 1404.
33. N. Zhang, X. Han, Y. Liu, X. Hu, Q. Zhao and J. Chen, *Adv. Energy Mater.*, 2014, **4**, 1401123.
34. Z. Y. Wang, D. Y. Luan, S. Madhavi, Y. Hu and X. W. Lou, *Energ. Environ. Sci.*, 2012, **5**, 5252.
35. F. Han, D. Li, W. C. Li, C. Lei, Q. Sun and A. H. Lu, *Adv. Funct. Mater.*, 2013, **23**, 1692.
36. J. L. Cheng, B. Wang, C. M. Park, Y. P. Wu, H. Huang and F. D. Nie, *Chem. Eur. J.*, 2013, **19**, 9866.
37. S. Q. Chen, P. Bao and G. X. Wan, *Nano Energy*, 2013, **2**, 425-434.
38. S. Yang, C. Cao, G. Li, Y. Sun, P. Huang, F. Wei and W. Song, *Nano Res.*, 2014, **7**, 1.
39. M. H. Chen, J. L. Liu, D. L. Chao, J. Wang, J. H. Yin, J. Y. Lin, H. J. Fan and Z. X. Shen, *Nano Energy*, 2014, **9**, 364.
40. H. L. Fei, Z. W. Peng, L. Li, Y. Yang, W. Lu, E. L. G. Samuel, X. J. Fan and J. M. Tour, *Nano Res.*, 2014, **7**, 502.
41. N. Li, Q. Zhang, J. Liu, J. Joo, A. Lee, Y. Gan and Y. D. Yin, *Chem. Commun.*, 2013, **49**, 5135.
42. P. Wu, N. Du, H. Zhang, J. X. Yu and D. R. Yang, *J. Phys. Chem. C*, 2010, **114**, 22535.
43. D. Larcher, C. Masquelier, D. Bonnin, Y. Chabre, V. Masson, J.-B. Leriche and J.-M. Tarascon, *J. Electrochem. Soc.*, 2003, **150**, A133.
44. X. L. Wu, Y. G. Guo, L. J. Wan and C. W. Hu, *J. Phys. Chem. C*, 2008, **112**, 16824.
45. S. L. Chou, J. Z. Wang, D. Wexler, K. Konstantinov, C. Zhong, H. K. Liu and S. X. Dou, *J. Mater. Chem.*, 2010, **20**, 2092.
46. W. Zhou, L. J. Lin, W. J. Wang, L. L. Zhang, Q. O. Wu, J. H. Li and L. Guo, *J. Phys. Chem. C*, 2011, **115**, 7126.
47. B. Sun, J. Horvat, H. S. Kim, W. S. Kim, J. Ahn and G. X. Wang, *J. Phys. Chem. C*, 2010, **114**, 18753.
48. L. Yu, S. Xi, C. Wei, W. Zhang, Y. Du, Q. Yan and Z. Xu, *Adv. Energy Mater.*, 2014, **4**, 1401517.
49. Y. Z. Su, S. Li, D. Q. Wu, F. Zhang, H. W. Liang, P. F. Gao, C. Cheng and X. L. Feng, *Acs Nano*, 2012, **6**, 8349.
50. W. M. Zhang, J. S. Hu, Y. G. Guo, S. F. Zheng, L. S. Zhong, W. G. Song and L. J. Wan, *Adv. Mater.*, 2008, **20**, 1160.
51. Y. Zhao, J. X. Li, C. X. Wu, Y. H. Ding and L. H. Guan, *Chempluschem*, 2012, **77**, 748.
52. Z. Y. Cai, L. Xu, M. Y. Yan, C. H. Han, L. He, K. M. Hercule, C. J. Niu, Z. F. Yuan, W. W. Xu, L. B. Qu, K. N. Zhao and L. Q. Mai, *Nano Lett.*, 2015, **15**, 738.
53. S. H. Choi, J. K. Lee and Y. C. Kang, *Nanoscale*, 2014, **6**, 12421.
54. Y. Z. Jiang, M. J. Hu, D. Zhang, T. Z. Yuan, W. P. Sun, B. Xu and M. Yan, *Nano Energy*, 2014, **5**, 60.